

# Self-organization of Nanostructures in Inorganic and Organic Semiconductor Systems\*\*

By Christian Teichert,\* Christian Hofer, and Gregor Hlawacek

*Semiconductor nanostructures – and in particular ensembles of them – are the prerequisites for the ongoing miniaturization in microelectronics. Since lithographic techniques become increasingly expensive and technologically complex, self-organization into quasiperiodic nanostructure arrays is an elegant alternative. Here, strain-induced pattern formation in SiGe/Si(001), ion bombardment induced self-organization of inorganic semiconductors, and crystallite ordering in oligophenylene films are presented as illustrative examples for nanostructure self-organization that is not at all restricted to semiconductor systems.*

## 1. Introduction

With the emergence of nanoscience and nanotechnology during the last years, there is a growing demand to efficiently fabricate nanostructured materials. Microelectronics with its ongoing miniaturization faced this challenge early and pioneered technologies to fabricate nanostructures. Since with shrinking dimensions the conventional “top down” approach using lithographic techniques becomes more and more expensive and technologically challenging, the “bottom up” approach – where single atoms or molecules spontaneously form nanostructures which self-organize into quasiperiodic arrays – is an elegant alternative. Thus, the exploration of self-organization phenomena at crystalline surfaces and in epitaxial films became an attractive research topic in the last decade.<sup>[1]</sup> Among the most active fields in this research area are strain driven self-organization in the intensively investigated inorganic semiconductor heteroepitaxy,<sup>[2]</sup> pattern formation due to low-energy ion erosion of semiconductor surfaces,<sup>[3]</sup> and the emerging field of nanostructure self-organization in crystalline organic semiconductor films.<sup>[4]</sup>

Here, we apply atomic-force microscopy (AFM) under ambient conditions to quantify the self-organization in several semiconductor systems. Usually standard silicon AFM tips with a half opening angle of 10° were used, but for high spatial resolution also plasma-sharpened high-density carbon

(HDC) tips and carbon nanotube (CNT) tips with half opening angles less than 5° and guaranteed tip radius of 5 nm were applied. Integral information on nanostructure arrangement and preferential size has been obtained by analyzing one- and two-dimensional power spectra calculated from AFM topographs containing 512 × 512 pixels. In order to obtain more accurate data, frequently larger AFM scans – providing better statistics – have been analyzed. (For details, the reader is referred to Chapters 2.1. and 2.2. of Ref.<sup>[2]</sup>). It should

[\*] Prof. C. Teichert, C. Hofer, G. Hlawacek  
Institute of Physics, Montanuniversität Leoben  
Franz Josef Str. 18, A-8700 Leoben, Austria  
E-mail: teichert@unileoben.ac.at

[\*\*] Support by Austrian Science Fund (FWF), Contract No. P14009 and FWF National Research Network “Interface controlled and Functionalised Organic Films” (S9707-N08), by the EC-Project NAMASOS (Nanomagnets by Self-Organisation, STRP 505854-1), and by the Federal Ministry of Education, Science and Culture of the Republic of Austria (bm:bwk) is acknowledged. We further thank K. Lyutovich, E. Kasper, T. Bobek, H. Kurz, A. Andreev, H. Sitter, and N.S. Sariciftci for collaboration and sample supply as well as S. Abermann, M. Xu, G. Fontalvo, M. Ramsey, and J. Ivanco for technical assistance.

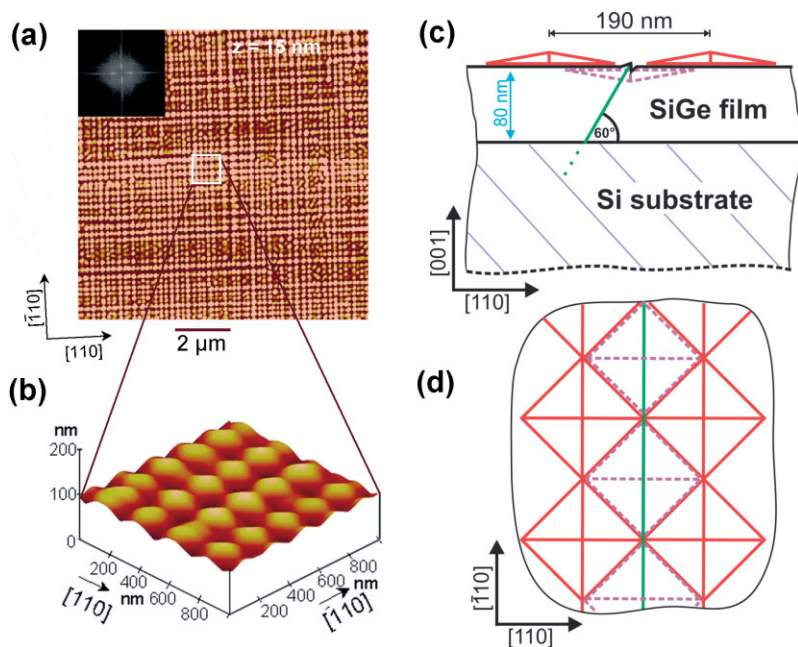


Fig. 1. Interplay of a misfit dislocation network with {105} faceted crystallites in an 80 nm SiGe film grown in two steps on Si(001). (a)  $10\ \mu\text{m} \times 10\ \mu\text{m}$  AFM image. Color scale range is 15 nm (z-scale). Inset: 2D power spectrum (calculated from a  $20\ \mu\text{m} \times 20\ \mu\text{m}$  image) ranging from  $-12.5\ \mu\text{m}^{-1}$  to  $12.5\ \mu\text{m}^{-1}$ . (b)  $1\ \mu\text{m} \times 1\ \mu\text{m}$  image in 3D presentation of the part marked in (a). Note that the vertical scale is exaggerated by a factor of two. (c) Cross sectional schematic view of the sample with a  $60^\circ$  misfit dislocation originating at the film substrate interface. (d) Top view of (c). (After Ref. [11])

be noted that the results are in general completed by structural investigations using x-ray diffraction and electron microscopy techniques to obtain additional structural information.<sup>[5]</sup> From the evolution of the patterns, the driving forces for the nanostructure self-organization are derived.

The paper is organized as follows. In Section 2, the spontaneous formation of a checkerboard pattern consisting of {105} faceted SiGe pyramids and pits on Si(001) is presented as an illustrative example for strain-induced self-organization in semiconductor heteroepitaxy. In Section 3, ion bombardment induced self-organization is compared for III-V and group IV semiconductors as well as ion erosion of already self-organized SiGe films is shown. In Section 4, a novel self-organization mechanism where para-sexiphenyl crystallites rearrange into well oriented nanofibers on mica(001) is described. In the final section, an outlook towards potential applications of self-organized semiconductor nanostructures is given.

## 2. Self-organization by an Interplay of Crystallite Formation with the Evolution of Misfit Dislocations

The heteroepitaxial growth of Ge or SiGe alloys on the technologically most relevant Si(001) surface – which proceeds in Stranski-Krastanov growth mode – is a model system for semiconductor heteroepitaxy.<sup>[2,6]</sup> Due to the 4 % larger lattice constant of Ge with respect to Si, the morphological evo-

lution is determined by strain relief. (For a detailed scenario of strain relief in this system see Ref.<sup>[2]</sup>) The most prominent morphological feature of strain relief is a coherently strained {105} faceted crystallite with rectangular base, the so called “hut cluster”.<sup>[7]</sup> These three-dimensional (3D) crystallites usually arrange in an interlocked array resulting in a broad size distribution. By growing a SiGe/Si superlattice, however, the crystallites self-organize laterally into a close-packed array of fourfold pyramids as a result of strain mediation through the Si spacer layer.<sup>[8]</sup> In a single SiGe layer, the pyramid-like crystallites can be aligned in  $\langle 110 \rangle$  directions due to an interplay with the  $60^\circ$  misfit dislocations that are introduced to finally relax a thick SiGe film.<sup>[9]</sup>

Here, it is shown that a dense network of such dislocations guides the {105} faceted SiGe pyramids into a self-organized checkerboard array. For this purpose, an 80 nm  $\text{Si}_{0.7}\text{Ge}_{0.3}$  film was grown by molecular beam epitaxy (MBE) in a two-stage process on Si(001). The process was originally designed to fabricate smooth strain relaxed “virtual SiGe substrates” for device applications<sup>[10]</sup> but may also result in corrugated SiGe films.<sup>[11]</sup> In the first stage, 30 nm  $\text{Si}_{0.7}\text{Ge}_{0.3}$

were grown under simultaneous  $\text{Si}^+$  ion bombardment at  $150^\circ\text{C}$ .<sup>[12]</sup> The subsequent 50 nm have been conventionally deposited at  $550^\circ\text{C}$ . The low temperature step leads to a high density of point defects which gives rise to the formation of a dense network of misfit dislocations when heating the substrate to the temperature of the second growth stage.<sup>[10]</sup> Figure 1 presents the resulting growth morphology together with a scheme that illustrates the crystallite self-organization. In the large-scale AFM image (Fig. 1(a)) it is visible that four-sided pyramids arrange in chains along the  $\langle 110 \rangle$  directions which cross each other. Analysis of the corresponding 2D power spectrum yields the periodicity of the faceted pyramids to be about 190 nm in  $\langle 110 \rangle$ . These ordered chains may extend over several micrometers. Frequently, adjacent chains touch each other as is shown in Fig. 1(b)) resulting in a checkerboard pattern of {105} faceted pyramids.<sup>[11]</sup> Cross-sectional line scans reveal that also the areas between the pyramids have a slope of about  $11^\circ$ , i.e., they are {105} faceted pits. In the ideal case the checkerboard array of pyramids and pits is formed by almost square {105} facets with an edge length of 95 nm.<sup>[11]</sup> The sketch in Fig. 1(c,d)) demonstrates the interplay between the crystallites and the dislocation network. The misfit dislocations (green) originating at the film substrate interface result in ridge trough structures with subnanometer height at the surface which guide the subsequently forming {105} faceted crystallites in two rows. The driving force for the pit formation in the areas between the pyramids is also strain relief. Although the areas with ideal checker-

board periodicity extend only across a few  $\mu\text{m}$ , the self-organized pattern can be found across the entire sample. Thus the proposed two stage growth procedure is an elegant and inexpensive way to pattern Si wafers on the nanometer scale.

### 3. Ion Bombardment Induced Pattern Formation on Semiconductor Surfaces

Also the destructive technique of low-energy ion erosion that is commonly used for surface cleaning in ultra-high vacuum experiments can result – rather unexpectedly – in spontaneous pattern formation on semiconductor surfaces.<sup>[3]</sup> Here, we present a summary of AFM based quantitative investigations of the temporal pattern evolution of semiconductor surfaces under normal incidence ion erosion. The promising results for  $\text{Ar}^+$  bombarded GaSb(001) surfaces are compared with noble gas ion erosion of the Si(001) surface as well as with ion bombardment of a nanofaceted SiGe film on Si(001).

#### 3.1. Self-organized dot Patterns on Compound Semiconductor Surfaces

Ion erosion on commercially available GaSb(100) substrates at a temperature of  $90^\circ\text{C}$  was carried out using a sputtered neutral mass spectrometer (SNMS) system with 500 eV  $\text{Ar}^+$  ions at an ion current density of about  $800 \mu\text{A}/\text{cm}^2$ . The

AFM measurements were performed *ex situ* for a series of samples with varying bombardment time.<sup>[13]</sup> An average sputter velocity of 2 nm/s was estimated from measuring the sputter depth with an interferometric profilometer. Figure 2 summarizes the results for sputter times ranging over four orders of magnitude. After a few seconds, there is just random roughening of the surface. At already 10 s, features with a preferential size of about 40 nm evolve as indicated by a ring in the 2D power spectral density (PSD) graph (Fig. 2(b)). Clear dot-like surface structures appear at an intermediate stage with the highest roughness (Fig. 2(c)). At sputter times of 150 s and beyond, a regular dot pattern with hexagonal order is observed. In Fig. 2(f-h)), high-resolution AFM images recorded with a CNT attached to a conventional AFM cantilever are presented.<sup>[14]</sup> The artificial color scale has been chosen to demonstrate the “dot”-like nature of the nanostructures in contrast to the faceted nanostructures in semiconductor heteroepitaxy. The initial features are rather shallow. In the intermediate stage, however, cone-like structures of up to 40 nm height are observed. In the ordered state, the structures have an almost hemispherical shape with a diameter of about 40 nm and 20 nm height. Fig. 2(i)) shows the evolution of the root mean square (rms) roughness  $\sigma$  with sputter time. In Regime I (up to 20 s), there is an exponential increase of  $\sigma$  due to the random roughening.<sup>[13]</sup> The highest roughness is observed between 50 s and 150 s (Regime II) where initial fluctuations in the surface removal (visible in Fig. 2(a)) result

in height fluctuations of the dots (see Fig. 2(c)). In the stationary Stage III, a constant  $\sigma$  value of about 6 nm is reached. A close look at Figs. 2(d,e) reveals that the hexagonal ordering in stage III occurs in domains of a few 100 nm diameter that are randomly oriented. The rather high degree of self-organization within a domain is reflected by the appearance of up to four narrow rings in the 2D-PSD (Fig. 2(d,e)). The diameter of the inner ring is related to the dot-dot separation. (Since the dots are close-packed, this value corresponds also to the dot diameter.) To quantify the size uniformity, it is convenient to analyse the radial PSD plots (see also Fig. 3).<sup>[13]</sup> The preferential dot diameter is deduced from the centre position of the first peak and its full width at half maximum (FWHM) indicates the width of the size distribution. The results are presented in Fig. 2(j). The high degree of self-organization is clearly indicated by the drop of the size fluctuation to a value of  $\pm 10\%$  for the 40 nm dots in Stage III.

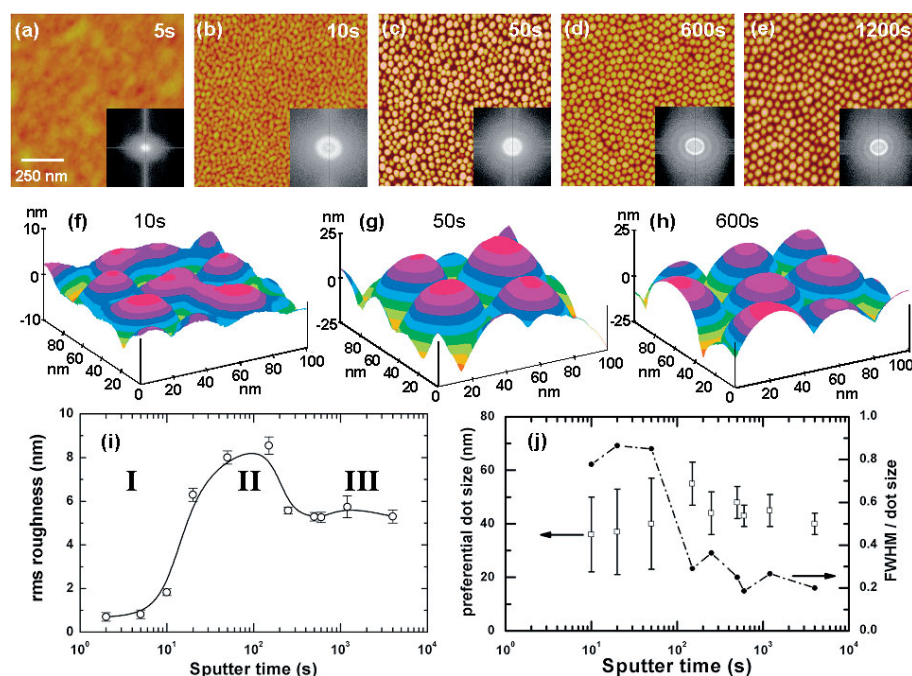


Fig. 2. Temporal evolution of surface morphology of 500 eV  $\text{Ar}^+$  ion eroded GaSb(100) under normal incidence. (a–e)  $1 \mu\text{m} \times 1 \mu\text{m}$  AFM images. z-scale: 25 nm. Insets: 2D power spectra (calculated from  $2 \mu\text{m} \times 2 \mu\text{m}$  images) ranging from  $-125 \mu\text{m}^{-1}$  to  $125 \mu\text{m}^{-1}$ . (f–h) 3D AFM topographs recorded with carbon nanotube AFM tips. In contrast to common presentations, the vertical scales in (g,h) are not exaggerated. (i) Evolution of surface roughness revealing three stages (I–III). (j) Preferential dot size with corresponding FWHM of the size distribution as error bars. Also the ratio of the preferential dot size to the FWHM is given as a function of sputter time. (After Refs. [13,14].)



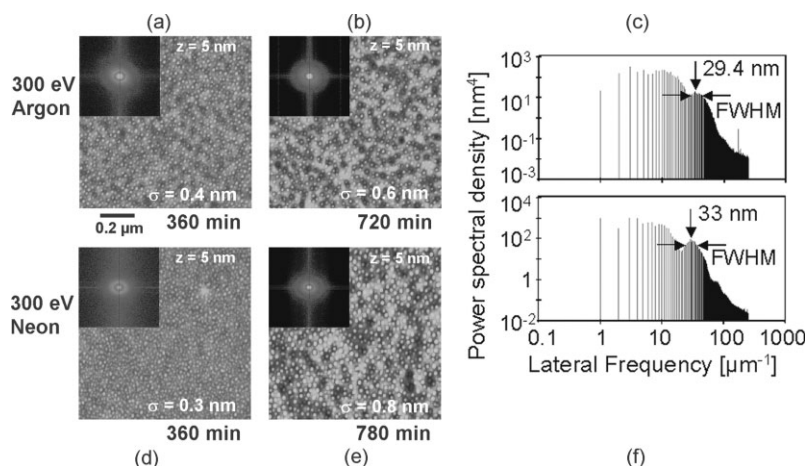


Fig. 3. Morphology evolution of ion eroded Si(001). Top row 300 eV Ar<sup>+</sup> ions, bottom row 300 eV Ne<sup>+</sup>. (a, b, d, e) 1 μm × 1 μm AFM images showing the resulting morphologies after the sputter times indicated. Insets: PSD of the corresponding AFM image, ranging from -250 μm<sup>-1</sup> to 250 μm<sup>-1</sup>. The corresponding rms roughness values  $\sigma$  and the z-scale values are given. (c, f) Resulting radial PSD for the larger sputter times. The vertical arrows indicate the predominant dot size.

It should be noted here that the ordering is independent of the substrate orientation: the same dot patterns are observed on ion eroded GaSb(111) as well as on amorphous GaSb films.<sup>[15]</sup> Also ion bombardment under oblique angles and simultaneous sample rotation (first observed for InP(111)) results in the same pattern.<sup>[16]</sup> These findings justify to use continuum theory to model the observed pattern formation: The Bradley-Harper (BH) theory predicts a temporal evolution of the surface morphology dependent on the erosion velocity, the surface tension, and surface diffusion. The concept of curvature dependent sputter yield proposes a stronger erosion of depressions compared to protrusions. Counteracting smoothing is induced by diffusion which includes thermal diffusion and erosion induced diffusion. This interplay between curvature dependent sputter yield and surface diffusion effects leads to a predominant feature size for normal ion incidence or to the formation of ripple patterns with a characteristic wavelength under oblique incidence.<sup>[17]</sup> A rather comprehensive agreement with the experimentally observed dot patterns under normal incidence has been obtained by simulations in the framework of the 2D damped Kuramoto-Sivashinski equation<sup>[18]</sup> which further includes angle dependent sputtering fluctuations due to the stochastic nature of the sputtering.

### 3.2. Dot Formation on Silicon

The successful pattern generation on compound semiconductors encouraged investigations of low energy ion erosion of Si(001) wafers. Although several different approaches have shown the possibility to produce nanostructured patterns on silicon by ion erosion,<sup>[19–21]</sup> the degree of ordering, however, is lower than in the case presented above for GaSb. Depend-

ing on the sputter parameters, sometimes – instead of dot-like patterns – craters form<sup>[22]</sup> or even a smoothing of the surface occurs.<sup>[23–24]</sup>

Here, we use normal incidence ion bombardment with Argon and Neon ions generated in an ISIS 3000 ion gun with an ion current density of 15 μA/cm<sup>2</sup> at 500 eV. The substrate temperature of the Si(001) samples, which were covered with a native oxide, was kept at about 40 °C. The silicon samples were fixed on the sample holder with two molybdenum wires and the irradiated area of the ion beam was larger than the size of the samples (12 mm × 6 mm). The dot density was determined by counting all dots within several 1 μm × 1 μm AFM images of different areas in the centre of the sample. The dot height is calculated as an average of several dots determined from line scans. The ion erosion in the ion energy range of 500 eV and below results in a dot pattern for both, Argon and Neon ions. Figure 3(a,b) shows AFM images of the resulting morphology after the erosion process with Argon ions. For a sputter time of 360 min the dot density is already 200 μm<sup>-2</sup> and the dot height is about 0.8 nm at an rms roughness of 0.4 nm. The lateral dot size was analysed by the radial PSD, which allows to determine the dominant structure size, in this case 27 nm (Fig. 3(c)). From the FWHM of the peak the uniformity of the structures is derived, which is ± 20 %. After twice the sputtering time the rms roughness increased to 0.6 nm and the dots gained in height (1.8 nm) and lateral size (29 nm) with an uniformity of ± 27 %. Also their density increased to about 330 μm<sup>-2</sup>. The longer sputter time caused large scale height fluctuations on which the dots are imposed. In Figure 3(b) one can observe that the dots are often surrounded by a ring-like area, which is lowered compared to the dots.

Neon was used to investigate a possible influence of the sputter gas. Ne has an atomic mass closer to silicon and might therefore induce larger damages. In Figure 3(d,e) the distribution of the dots for sputter times of 360 min and 780 min is shown. At 360 min the dominant dot size is 26 nm with a uniformity determined from the FWHM of ± 38 %. The dot density is about 400 μm<sup>-2</sup> and their height varies between 0.3 nm and 1.2 nm at an rms roughness of 0.3 nm. The increased sputter time of 780 min leads to an increase of the structure size to 33 nm with an improved uniformity of ± 18 % (Fig. 3(f)). Compared to Ar<sup>+</sup> bombardment, the ordering for Ne<sup>+</sup> ions is better. This might be addressed to the fact that for Ne the ratio of ion to target mass is closer to one.

One possible reason for the observed dot formation could be the presence of the Mo wires with which the samples were fixed. Since the wires are also bombarded by the noble gas ions, Mo atoms sputtered off the wires can be spread on the Si surface. Recently such a seeding with Mo was found to induce a dot pattern.<sup>[25]</sup> There, approximately 5 % Mo covering of the surface were detected by Auger Electron Spectroscopy

(AES) and X-ray photoelectron spectroscopy. To clarify this possible effect of the wires, AES measurements were carried out (not shown here), which did not reveal traces of molybdenum within the detection range of 1 % on the sample surface, except beneath the areas covered by the Mo wires. Although the AES measurements could not reveal Mo on the surface, there are high-resolution transmission electron microscopy measurements planned to reveal any traces of Mo below 1 %. AFM measurements of Si substrates which were fixed without Mo wires revealed a much lower density and height of the dots with irregular arrangement and an rms roughness of 0.2 nm. Thus, we can assume that smallest traces of Mo are already responsible for the dot formation. The underlying process might be local molybdenum silicide formation with reduced sputter yield compared to Si.<sup>[25]</sup> The molybdenum silicide at the surface therefore might shield the underlying Si from sputtering, thus acting like glacier tables. Nevertheless, we have to state that the patterns in ion bombarded Si are much less uniform than in GaSb or other compound semiconductors.

Although the phenomena leading to the nanostructure formation by normal incidence ion erosion are qualitatively understood in the framework of continuum elasticity theory, the underlying atomic processes and the role of possible stress are not completely understood until now. One reason for the better ordering in compound semiconductors might be stress due to preferential sputtering and segregation. Just recently, the issue of evolving stress<sup>[26]</sup> as well as the influence of the substrate temperature have been addressed.<sup>[27]</sup>

### 3.3. Ion Bombardment Induced Pattern Transformation in Self-organized SiGe Films

One might ask how an already pre-structured surface behaves under ion bombardment. Therefore we have studied the evolution of the morphology of pre-structured surfaces (see Fig. 1(a)) during low energy ion erosion.<sup>[28]</sup> The bombardment conditions were the same as in Section 3.1. For Ar<sup>+</sup> ion erosion of the self-organized SiGe checkerboard pattern of pyramids and pits (see Section 1) the results are summarized in Figure 4. The sputter depth was measured as height difference between eroded sample area and untreated area with an interferometric profilometer. Figure 4(a-c) summarizes the evolution of the morphology with increasing sputter time and therefore increasing sputter depth for the ion energy of 500 eV. The first sputter experiment with a sputter depth of 340 nm (Fig. 4(a,g)) reaches already the sili-

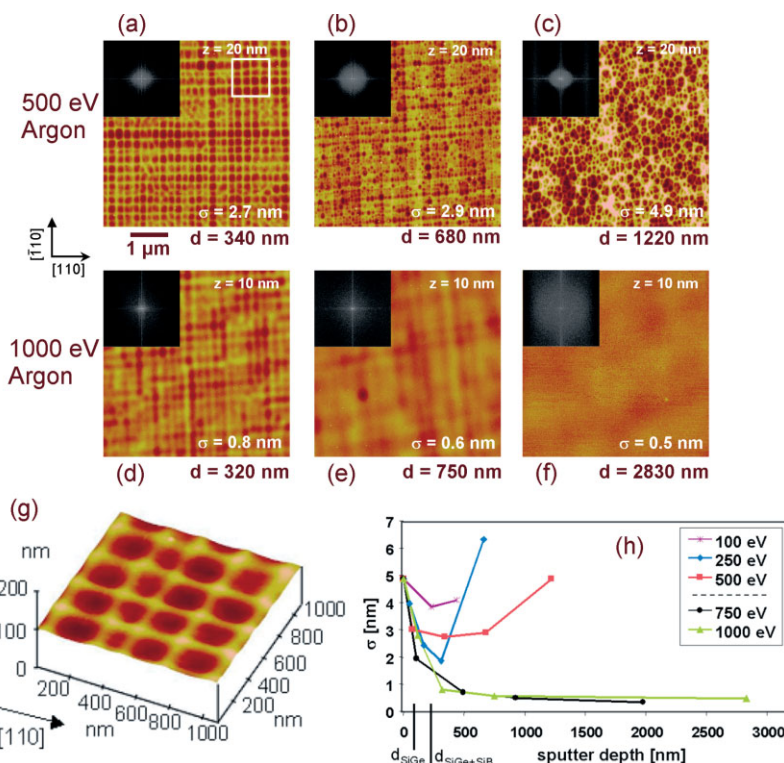


Fig. 4. Morphology evolution of self-organized SiGe checkerboard pattern under Ar<sup>+</sup> ion erosion. (a–f) 5  $\mu\text{m} \times 5 \mu\text{m}$  AFM images with corresponding 2D PSD graphs, ranging from  $-50 \mu\text{m}^{-1}$  to  $50 \mu\text{m}^{-1}$ . The sputter depth  $d$ , the  $z$ -scale range, and the resulting rms roughness  $\sigma$  are indicated. (g) 3D image showing a zoom into the area marked in (a) to compare it with the starting morphology (Fig. 1(b)). (h) Evolution of rms roughness  $\sigma$  with increasing sputter depth. (After Ref. [28].)

con bulk of the sample. The pattern is smeared out but still resembles the original morphology. A comparison of the high-resolution AFM images in Figure 1(b) and Figure 4(g) shows the transformation of the {105} pyramidal pits with edges along the  $\langle 100 \rangle$  directions (see Fig. 1(d)) into shallow troughs with edges along  $\langle 110 \rangle$ . The ridges between the troughs can be identified as the remainders of the pyramidal chains. Due to the shallower structures, the roughness is decreasing from 4.9 nm for the starting morphology to 2.7 nm at 340 nm sputter depth. The transformation of the pyramidal pits into more shallow troughs agrees with the prediction of the curvature dependent sputter yield of the BH theory. A detailed analysis of a SiGe sample with less dense arrangement of pyramids and pits showed more evidence for this behaviour.<sup>[28]</sup>

When the ion erosion reaches higher sputter depths (Fig. 4(b,c)), a sudden change in the morphology is seen. Small sputter craters develop, which have a diameter of about 70 nm and are about 20 nm deep surrounded by a network of ridges. The rms roughness is increasing to 2.9 nm, and this trend continues at larger sputter depths. The insets in Figure 4(a–c) show the corresponding 2D PSD graphs which illustrate the increasing disorder of the structures.

Completely different is the evolution of the morphology with ion energies higher than 500 eV. In the case of an ion energy of 1000 eV three stages of the vanishing pattern are shown in Figure 4(d–f). Again, in the beginning of sputtering

(Fig. 4(d)) the original pattern is still visible, but with increasing sputter depth the pattern vanishes. The smoothing causes a decrease of the rms roughness to 0.5 nm at a sputter depth of 2830 nm (Fig. 4(f)).

In Figure 4(h) the rms roughness  $\sigma$  is presented as a function of the sputter depth for different  $\text{Ar}^+$  ion energies. The comparison between different ion-energies reveals two clearly distinguishable regimes of ion erosion, one below and one above 500 eV. For ion energies of 500 eV and below the pattern is preserved at first, followed by disordered craters and increased roughness. Higher ion energies lead to a vanishing of the pattern, which is also reflected by the 2D PSD graphs calculated from the corresponding AFM images in Figure 4(d–f).

This morphology evolution with two distinct energy regimes was also found for other SiGe substrates. The starting morphologies varied from shallow {1 1 1} ( $7.3^\circ$  slope) to rather steep {113} ( $25.2^\circ$  slope) faceted mesas, with varying arrangement and density of the nanostructures.<sup>[29]</sup> Although the size of the starting features determines the subsequent structure sizes, the morphologies in the low energy ion erosion regime show in all cases a dense network of sputter craters with varying diameters at high sputter depths. Ion energies above the threshold value, which is again between 500 eV and 750 eV, result in a vanishing of the pattern.

#### 4. Crystallite Self-organization in Organic Semiconductor Films

Organic semiconductor materials have shown potential for the production of inexpensive and flexible electronic and optoelectronic devices like organic thin film transistors (OTFT), organic light emitting diodes (OLED), and even lasers and

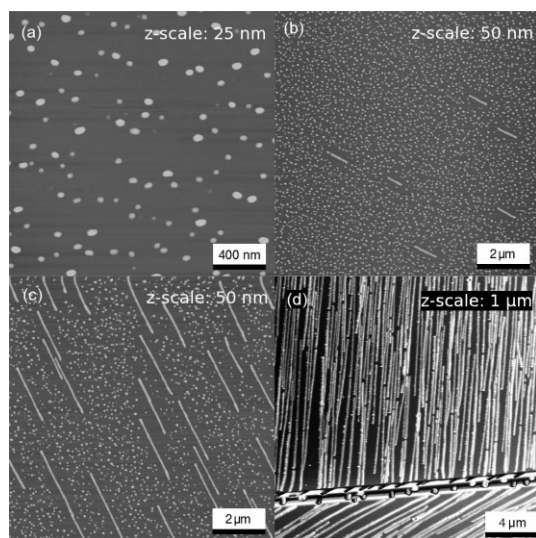


Fig. 5. Growth stages for a 6P thin film grown by HWE on mica(001). AFM images of the early growth stage (a), intermediate stages (b,c) and the final stage (d). Please, note the different scale bars and z-scale ranges. (After Ref. [34].)

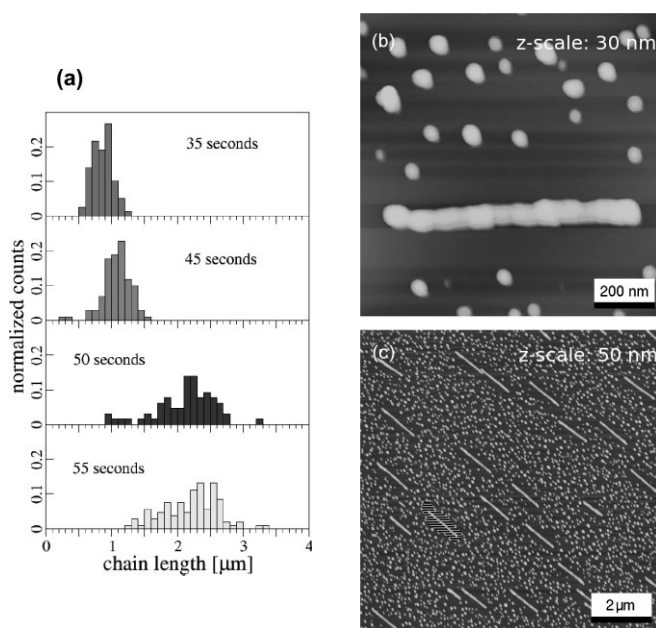


Fig. 6. Detailed analysis of chain growth during the intermediate stage of 6P on mica(001). (a) chain length histograms for different deposition times. (b)  $1 \mu\text{m} \times 1 \mu\text{m}$  AFM scan revealing the internal structure of a single chain. (c) Film morphology after 45 sec. Each chain is surrounded by a depleted zone as the one shaded in green.

wave guides.<sup>[30,31]</sup> These materials offer the utilization of self-organization processes due to the anisotropy of their building blocks, the molecules. In contrast to the classical semiconductor heteroepitaxy which is controlled by the formation of covalent bonds between the substrate and the film atoms, the epitaxial growth of organic semiconductor thin films is determined by weaker interactions like van der Waals forces, dipole-dipole, and coulomb interactions. In the case of oligophenylene films, e.g., it has been found that despite the weak interaction between the molecules and the substrates the film morphology is significantly determined by the substrate geometry.<sup>[4]</sup> The obvious size difference between the building blocks of the film and the substrate in combination with the anisotropy of the building blocks is important to understand – and finally to control – the morphology and structure of the resulting films.

Here, a self-organization phenomenon occurring during growth of the conjugated oligomer para-sexiphenyl (6P,  $\text{C}_{36}\text{H}_{26}$ ) on mica(001) is investigated. The films were deposited by hot wall epitaxy (HWE) at  $90^\circ\text{C}$  (for details see Ref. [32]). Figure 5 shows the different stages in the growth of 6P thin films on mica(001). The initial morphology (Fig. 5(a)) is characterized by small randomly distributed crystallites with  $50 \text{ nm} \times 100 \text{ nm}$  lateral extension and 20 nm height. With further growth, suddenly well oriented chains of crystallites appear (Fig. 5(c,d)). The final morphology (Fig. 5(d)) is made up of micrometer long 1D chains of small crystallites. The orientation of the chains is mediated by a dipole-dipole interaction between the mica(001) surface and the quadrupole moment of the 6P molecule. The several micrometer long 6P chains, therefore, reflect the threefold symmetry of the under-



lying substrate. Due to some peculiarities of the muscovite  $2M_1$  unit cell only two of the three orientations are possible. An odd number of cleavage steps reveals this characteristic of the mica(001) surface, as the chain orientation turns by  $120^\circ$  (Fig. 5(d)).<sup>[32,33]</sup> The intermediate growth stage (Fig. 5(b,c)), is characterized by a coexistence of chains and crystallites. In Figure 6, further experimental details are presented that helped to develop a scenario for the self-organization of crystallites into chains.<sup>[34]</sup> The chain length distribution in Figure 6(a) reveals the increase of chain length with the amount of deposited material and the fact that the distributions are rather narrow, in particular for small growth time, where no chain coalescence occurs. Most important, there is an increasing threshold length of about 500 nm, below that no chains exist. The small scale AFM image (Fig. 6(b)) of an individual chain reveals the internal chain structure indicating that the chain has been formed by a rearrangement of individual crystallites. A second proof for this statement is the observation of a depleted or denuded zone around the chains. In Figure 6(c) this zone around one of the chains is marked. The number of crystallites found in an undisturbed area equal to that of the typical denuded zone is sufficient to build a single chain.

The question arises what mediates the self-organization of the crystallites? We proposed elsewhere that a critical density of crystallites induces a local linear defect in the wetting layer

which forms prior to the crystallites.<sup>[34]</sup> The influence of the defects in the wetting layer, which act as nucleation centres for the formation of the chains, can also be seen from an annealing experiment shown in Figure 7. Here, two films were grown under identical conditions, but the second film (Fig. 7(b)) experienced an annealing step at the growth temperature for 10 min after growth. The corresponding chain length histograms presented in Figure 7(c,d) change significantly due to the annealing. The double peak in Figure 7(d) can be explained with an increase of chain length for the already existing chains (right peak) and the formation of new short chains (left peak). The incorporation of crystallites into either existing chains, and thereby increasing their length, or new ones is also reflected in the respective feature density. While the chain density increases from  $0.35 \mu\text{m}^{-2}$  to  $0.50 \mu\text{m}^{-2}$  the crystallite density decreases slightly from  $18.5 \mu\text{m}^{-2}$  to  $18.0 \mu\text{m}^{-2}$ . In addition to these quantitative changes due to the annealing, the annealed sample shows a higher probability to find two or more chains aligned along a straight line. Especially the newly built short chains show a significant tendency to line up with longer chains from the initial growth. This effect can be attributed to the linear defect network formed by the initially built chains. When deposition is stopped, no more new crystallites are formed but more time is given for existing crystallites to reduce the strain in the system by either attaching to an existing chain or by forming a

new one. This new chain must be formed along an already existing defect, and is therefore lined up with an existing chain. All the experimental details presented support the assumption that the crystallites – consisting of about 140 000 molecules each – rearrange as entities.<sup>[34]</sup> In situ growth experiments are planned to verify this statement.

It should be noted here that growth of the same molecule results on a variety of substrates in self-organized nanostructure arrays. On Al(111) 6P forms crystallites that arrange star-like in 6 different directions<sup>[35,4]</sup> whereas on KCl(001)<sup>[36]</sup> and  $\text{TiO}_2(110)$ <sup>[37]</sup> needle-like crystallites with lengths of several 100 nm till some  $\mu\text{m}$  arrange along the substrates' close-packed directions. For the latter case it could be shown that not only the interplay with the substrate geometry determines pattern symmetry but also the change in growth temperature significantly influences structure, size, and shape of the resulting nanostructures.<sup>[4]</sup>

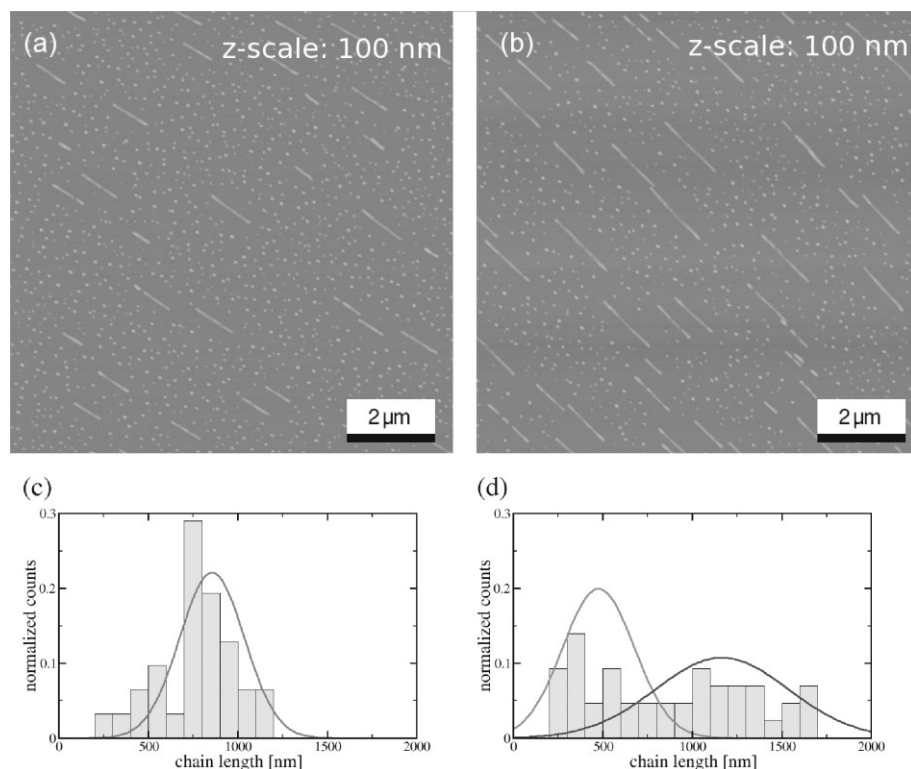


Fig. 7. Annealing of a 6P film on mica(001) at the growth temperature of  $90^\circ\text{C}$ . a,b)  $10 \mu\text{m} \times 10 \mu\text{m}$  AFM images of an as grown film and an annealed film, respectively. c,d) Corresponding chain length distributions.

## 5. Outlook to Potential Applications

At this point, the question arises if one can benefit from self-organizing semiconductor systems for potential applications. The classical application are self-organized "quantum dots" for light emitting diodes and semiconductor lasers.<sup>[1,38]</sup> In quantum dots, a confinement of the charge carriers in all three dimensions results in discrete energy levels. Besides the restriction in dimension, for quantum dot applications the ensembles of self-organized semiconductor nanostructures should exhibit a high areal density and a sufficient size uniformity which should be at least  $\pm 10\%$ . While group IV materials have the disadvantage of being indirect semiconductors, most promising for quantum dot applications are self-organized III–V heteroepitaxial nanostructures.<sup>[38]</sup> Also, the ion-bombardment induced GaSb nanostructures – which deserve due to their shape (see Fig. 2(h)) the term "dot" most – show in principle quantum dot properties.<sup>[3]</sup> However, due to the sputter damage resulting in an about 2 nm thick amorphous layer,<sup>[15]</sup> the efficiency of devices fabricated by such a strategy will be probably too low. For the crystalline para-sexiphenyl films, however, potential for devices like organic thin film transistors<sup>[39]</sup> and organic light emitting diodes<sup>[40,41]</sup> has already been demonstrated. In particular for the self-organized 6P nanofibers on mica, also coherent random lasing in the deep blue spectral range has been found.<sup>[42]</sup> To evaluate the electric properties of these one-dimensional 6P crystallite chains on the nanometer scale, conducting atomic-force microscopy<sup>[43]</sup> measurements are under way.

A second – rather unconventional – application is based on the fact that the inorganic heteroepitaxial and ion eroded semiconductor nanostructures cover the entire semiconductor wafer and represent therefore comparable inexpensive, large-area templates for subsequent deposition of other materials which might not show self-organizing behaviour themselves. Such materials range from proteins<sup>[44]</sup> and carbon nanotubes<sup>[45]</sup> to magnetic thin films.<sup>[46]</sup> In order to fabricate arrays of individual nanomagnets by this template technique, two strategies are imaginable: normal incidence deposition and grazing incidence deposition. For the first case, one could either utilize possible preferential nucleation, e.g., in the pits of the checkerboard pattern presented in Figure 1 and in the troughs shown in Figure 4, or curvature dependent deposition rates,<sup>[47]</sup> e.g., on the dot like pattern shown in Figure 2. The second case utilizes preferential deposition on the facets facing the deposition source and shadowing of the remaining areas. By this way, a large-area array of Co nanomagnets with uniaxial anisotropy has been obtained on a nanofaceted SiGe template.<sup>[48]</sup> By x-ray magnetic circular dichroism photoemission electron microscopy (XMCD-PEEM) it could be shown that such nanomagnets are indeed single domain, but also magnetically coupled.<sup>[49]</sup> Once these template techniques have proven to provide high-density arrays of uncoupled nanomagnets, the – for magnetic data storage applications so far insufficient template periodicity – might be obtained by the combination of self-organization phenomena with man-

made restructuring. Such hybrid techniques where "bottom up" meets "top down" have been successfully demonstrated recently.<sup>[50,51]</sup>

Finally, it should be mentioned that the self-organization phenomena illustrated in this review are by no means restricted to semiconductor systems. The mechanisms based on strain relief can be exploited also in other thin film systems to form spontaneously nanostructured surfaces with, e.g., tailored wetting behaviour and customized tribological properties.

- [1] V. A. Shchukin, D. Bimberg, *Rev. Mod. Phys.* **1999**, 71, 1125.
- [2] C. Teichert, *Phys. Rep.* **2002**, 365, 335.
- [3] S. Facsko, T. Dekorsy, C. Koerd, C. Trappe, H. Kurz, A. Vogt, H. L. Hartnagel, *Science* **1999**, 285, 1551.
- [4] G. Hlawacek, C. Teichert, A. Y. Andreev, H. Sitter, S. Berkebile, G. Koller, M. G. Ramsey, R. Resel, *Phys. Stat. Solidi a* **2005**, 202, 2376.
- [5] J. Stangl, V. Holy, G. Bauer, *Rev. Mod. Phys.* **2004**, 76, 725.
- [6] J.-M. Baribeau, N. L. Rowell, D. J. Lockwood, *J. Mater. Res.* **2005**, 20, 3278.
- [7] Y.-W. Mo, D. E. Savage, B. S. Swartzentruber, M. G. Lagally, *Phys. Rev. Lett.* **1990**, 65, 1020.
- [8] J. Tersoff, C. Teichert, M. G. Lagally, *Phys. Rev. Lett.* **1996**, 76, 1675.
- [9] D. E. Jesson, K. M. Chen, S. J. Pennycook, T. Thundat, R. J. Warmack, *Science* **1995**, 268, 1161.
- [10] E. Kasper, S. Heim, *Appl. Surf. Sci.* **2004**, 224, 3.
- [11] C. Teichert, C. Hofer, K. Lyutovich, M. Bauer, E. Kasper, *Thin Solid Films* **2000**, 380, 25.
- [12] M. Bauer, M. Oehme, K. Lyutovich, E. Kasper, *Thin Solid Films* **1998**, 336, 104.
- [13] T. Bobek, S. Facsko, H. Kurz, T. Dekorsy, M. Xu, C. Teichert, *Phys. Rev. B* **2003**, 68, 085324.
- [14] M. Xu, C. Teichert, *Physica E* **2005**, 25, 425.
- [15] S. Facsko, T. Bobek, H. Kurz, T. Dekorsy, S. Kyrsta, R. Cremer, *Appl. Phys. Lett.* **2002**, 80, 130.
- [16] F. Frost, A. Schindler, F. Bigl, *Phys. Rev. Lett.* **2000**, 85, 4116.
- [17] R. Bradley, J. M. E. Harper, *J. Vac. Sci. Technol. A* **1988**, 6, 2390.
- [18] S. Facsko, T. Bobek, A. Stahl, H. Kurz, T. Dekorsy, *Phys. Rev. B* **2004**, 69, 153412.
- [19] R. Gago, L. Vazquez, R. Cuerno, M. Varela, C. Ballesteros, J. M. Albella, *Appl. Phys. Lett.* **2001**, 78, 3316.
- [20] F. Ludwig, C. R. Eddy, O. Malis, R. L. Headrick, *Appl. Phys. Lett.* **2002**, 81, 2770.
- [21] B. Ziberi, F. Frost, B. Rauschenbach, T. Höche, *Appl. Phys. Lett.* **2005**, 87, 033113.
- [22] B. Ziberi, F. Frost, M. Tartz, H. Neumann, B. Rauschenbach, *Thin Solid Films* **2004**, 459, 106.
- [23] F. Frost, R. Fechner, B. Ziberi, D. Flamm, A. Schindler, *Thin Solid Films* **2004**, 459, 100.



- [24] J. C. Kim, J.-Y. Ji, J. S. Kline, J. R. Tucker, T.-C. Shen, *Appl. Surf. Sci.* **2003**, 220, 293.
- [25] G. Ozaydin, A. S. Özcan, Y. Wang, K. F. Ludwig, H. Zhou, R. L. Headrick, D. P. Siddons, *Appl. Phys. Lett.* **2005**, 87, 163104.
- [26] N. Kalyanasundaram, M. C. Moore, J. B. Freund, H. T. Johnson, *Acta Mater.* **2006**, 54, 483.
- [27] R. Gago, L. Vázquez, O. Plantevin, J. A. Sánchez-García, M. Varela, M. C. Ballesteros, J. M. Albella, T. H. Metzger, *Phys. Rev. B* **2006**, 73, 155414.
- [28] C. Hofer, S. Abermann, C. Teichert, T. Bobek, H. Kurz, K. Lyutovich, E. Kasper, *Nucl. Instrum. Meth. B* **2004**, 216, 178.
- [29] C. Hofer, C. Teichert, M. Wächter, T. Bobek, K. Lyutovich, E. Kasper, *Superlattice Microst.* **2004**, 36, 281.
- [30] N. S. Sariciftci, A. J. Heeger, in *Handbook of Org. Conductive Mol. and Polym.*, John Wiley & Sons, **1997**, 413.
- [31] H. E. Katz, A. Dodabalapur, Z. Bao, in *Handbook of Oligo- and Polythiophenes*, Wiley-VCH, Weinheim **1999**, 459.
- [32] A. Andreev, G. Matt, C. J. Brabec, H. Sitter, D. Badt, H. Seyringer, N. S. Sariciftci, *Adv. Mater.* **2000**, 12, 629.
- [33] H. Plank, R. Resel, A. Andreev, N. S. Sariciftci, H. Sitter, *J. Cryst. Growth* **2002**, 237–239, 2076.
- [34] C. Teichert, G. Hlawacek, A. Y. Andreev, H. Sitter, P. Frank, A. Winkler, N. S. Sariciftci, *Appl. Phys. A* **2006**, 82, 665.
- [35] R. Resel, I. Salzmänn, G. Hlawacek, C. Teichert, B. Koppelhofer, B. Winter, J. Krenn, J. Ivanco, M. G. Ramsey, *Org. Electron.* **2004**, 5, 45.
- [36] A. Y. Andreev, A. Montaigne, G. Hlawacek, H. Sitter, C. Teichert, *J. Vac. Sci. Technol. A* **2006**, 24, 1660.
- [37] G. Koller, S. Berkebille, J. R. Krenn, G. Tzvetkov, G. Hlawacek, O. Lengyel, F. P. Netzer, C. Teichert, R. Resel, M. G. Ramsey, *Adv. Mater.* **2004**, 16, 2159.
- [38] V. A. Shchukin, N. N. Ledentsov, D. Bimberg, *Epitaxy of Nanostructures*, Springer, Berlin **2004**.
- [39] D. J. Gundlach, Y.-Y. Lin, T. N. Jackson, D. G. Schlom, *Appl. Phys. Lett.* **1997**, 71, 3853.
- [40] H. Yanagi, S. Okamoto, T. Mikami, *Synthetic Met.* **1997**, 91, 91.
- [41] G. Leising, S. Tasch, W. Graupner, in *Handbook of Conducting Polym.*, Dekker, New York **1997**, 847.
- [42] A. Andreev, F. Quochi, F. Cordella, A. Mura, G. Bongiovanni, H. Sitter, G. Hlawacek, C. Teichert, N. S. Sariciftci, *J. Appl. Phys.* **2006**, 99, 034305.
- [43] S. Kremmer, C. Teichert, E. Pischler, H. Gold, F. Kuchar, M. Schatzmayr, *Surf. Interf. Anal.* **2002**, 33, 168.
- [44] M. Riedel, B. Müller, E. Wintermantel, *Biomaterials* **2001**, 22, 2307.
- [45] F. Granone, V. Mussi, A. Toma, S. Orlanducci, M. L. Terranova, C. Boragno, F. B. de Mongeot, U. Valbusa, *Nucl. Instrum. Meth. B* **2005**, 230, 545.
- [46] C. Teichert, *Appl. Phys. A* **2003**, 76, 653.
- [47] M. Albrecht, G. Hu, I. L. Guhr, T. C. Ulbrich, J. Boneberg, P. Leiderer, G. Schatz, *Nat. Mater.* **2005**, 4, 203.
- [48] C. Teichert, J. Barthel, H. P. Oepen, J. Kirschner, *Appl. Phys. Lett.* **1999**, 74, 588.
- [49] A. M. Mulders, A. Fraile Rodríguez, D. Arvanitis, C. Hofer, C. Teichert, M. Á. Niño, J. Camarero, J. J. de Miguel, R. Miranda, K. Lyutovich, E. Kasper, S. Heun, A. Locatelli, *Phys. Rev. B* **2005**, 71, 214422.
- [50] J. Choi, K. Nielsch, M. Reiche, R. B. Wehrspohn, U. Gösele, *J. Vac. Sci. Technol. B* **2003**, 21, 763.
- [51] Z. Y. Zhong, G. Bauer, *Appl. Phys. Lett.* **2004**, 84, 1922.